



Theoretical Analysis of Crack Propagation Measurement for Brittle Materials Based on Virtual Principal Strain Field

Liuning Gu¹ · Xinxing Shao¹

Received: 13 January 2022 / Revised: 22 March 2022 / Accepted: 23 March 2022 / Published online: 21 April 2022
© The Chinese Society of Theoretical and Applied Mechanics 2022

Abstract

The measurement of crack propagation is crucial for revealing the fracture mechanical properties of materials and structures. Based on the virtual principal strain field and Steger's algorithm, an accurate and automatic method has been proposed for measuring the geometric parameters of crack propagation. The measured geometric parameters of crack propagation include the width, length, and tip location of each crack. The mechanism of the crack-induced virtual principal strain field and the effects of subset, step, and strain window size are analyzed and discussed theoretically. The effectiveness of the derived theoretical equations is verified by the simulation experiments. According to the theoretical equations, it is determined that the distribution of the virtual principal strain field near the crack is similar to the grayscale distribution of the laser fringe image with optimized calculation parameters. Experiments are further conducted to validate the effectiveness of the derived equations. With the optimized calculation parameters, the minimum crack that can be measured is approximately 0.0362 pixel in the laboratory environment, while the measurement error of the crack width is less than 0.025 pixel for two-dimensional digital image correlation (DIC) and 0.020 pixel for three-dimensional DIC.

Keywords Crack propagation · Brittle materials · Digital image correlation · Virtual principal strain · Steger's algorithm

1 Introduction

The measurement of crack propagation is significant in revealing the fracture mechanical properties of materials and structures. Presently, the method of tracing the positions of cracks on an object surface is mainly the conventional manual detection method based on vision and marker pens. With respect to the width of cracks on the object surface, equipment based on an optical microscope with high measuring precision is utilized to measure the width of discrete points of the fine cracks [1]. Technologies such as demountable mechanical strain gauges and optical tracking marks [2] can also provide information on the relative displacement of finite isolated points, but these methods may not achieve the expected results when the measuring points are insufficient or the expected location of cracks is uncertain.

Recently, the method of surface crack identification based on digital image processing has developed a lot. Image-based

measurements usually segment cracks with integer-pixel accuracy from images because of the different grayscale between cracks and a brighter background. Compared with conventional methods such as manual observation, the efficiency of the image-based methods has improved significantly. Image-based methods can be roughly divided into the following categories:

1. the algorithm for crack identification based on the space domain, which utilizes methods and theories to measure cracks, such as threshold segmentation and edge detection [3];
2. the algorithm for crack identification based on the frequency field, which applies the wavelet transform [4], beamlet transform [5], contourlet transform [6], and other tools to identify cracks;
3. the algorithm for crack identification based on deep learning [7–9].

Among these image-based methods, the crack identification based on deep learning has recently attracted significant attention, and the crack identification accuracy has greatly improved. Ni et al. [7] utilized the multiscale feature fusion

✉ Xinxing Shao
xinxing.shao@seu.edu.cn

¹ Department of Engineering Mechanics, School of Civil Engineering, Southeast University, Nanjing 211189, China

network to realize the segmentation of cracks in integer pixel. Qin et al. [8] proposed deep convolutional neural networks (CNNs) based on SegNet and realized crack identification under the complex background. Cha et al. [9] utilized the CNN to identify cracks. However, the method based on deep learning usually requires a large amount of data to train an available model at high cost. The image-based method of crack identification is mainly utilized to detect static cracks on architectural surfaces such as bridges, roads, and buildings. When there is too much interference on the cracked surface, the accurate identification of cracks will be significantly influenced. In addition, the image-based method cannot measure the width of small cracks precisely, especially when the imaged crack is less than one pixel. Therefore, it is difficult to measure the crack propagation of materials at an early stage in a dynamic process.

In contrast to the image-based method, the digital image correlation (DIC) method with sub-pixel accuracy has been utilized to reconstruct the displacement field with discontinuities including cracks. The DIC method was proposed in the early 1980s [10–12]. After decades of development, it has been widely used in civil engineering, biomedical engineering, material science, and other fields owing to its advantages of non-contact, non-destructive and full-field measurement with high accuracy [13–18]. Poissant et al. [19] and Hassan et al. [20] proposed different subset-splitting methods, both of which hypothesized that a straight crack line traverses the selected subset and splits the subset into two parts. Réthoré et al. [21, 22] introduced the finite element method into DIC and described the discontinuous displacement with the shape functions enriched by the Heaviside function. Both methods mentioned above seem to be time consuming and complex in algorithms. Pan [23] set thresholds for the subset correlation coefficient calculated by DIC to determine the position of discontinuous parts. However, an obvious drawback of this method is the failure to detect small cracks. In short, these studies focused on the high-accuracy displacement calculation near the cracks and did not provide a solution to measure the geometric parameters of crack propagation.

Without reconstructing the displacement field near cracks, a few scholars utilized the strain field calculated by DIC to observe the fracture process of rocks, concrete, and other materials, because distinct strain fields are usually observed to be related to crack propagation. A few researchers quantitatively obtained detailed information such as the crack location, crack width and length of cracks. Yuan et al. [24] observed the crack growth process of asphalt concrete in a fracture test. Allam et al. [25] utilized DIC and acoustic emission techniques to study the effect of structural size on the cracking of reinforced concrete. The cracks were identified by the discontinuities of the object surface's displacements or the principal tensile strains. Ruocci et al. [26, 27] proposed an approach that the cracks were located at a local maximum of

horizontal strains. Shih et al. [28] utilized the von Mises strain field to detect and identify the early crack development. It is an inspiring work to use virtual strain field for crack detection. This method was further applied to cracking mapping on confined masonry walls [29] and prestressed concrete [30]. However, in these studies, crack distribution was only analyzed qualitatively, but not quantitatively [28–30]. Recently, Gehri et al. [31] proposed an automatic method for extracting the crack centerline based on morphological corrosion and expansion, as well as the virtual strain field, and some quantitative analysis is obtained. However, this method [31] is highly dependent on the preset threshold. In our previous work, an accurate and automatic method has been proposed for measuring the geometric parameters of crack propagation based on the virtual principal strain field and Steger's algorithm [32]. The method of obtaining crack information using a virtual principle strain field is simple and efficient. However, the mechanism of crack-induced virtual principal strain field hasn't been covered [28–32]. There is no theoretical analysis on the mechanism of crack-induced virtual principal strain field to date, and further research on the selection of optimized calculation parameters is also needed.

This study solves the aforementioned problems by reasonably simplify the displacement fields near Mode I and II cracks in brittle materials, and theoretically derived the mathematical forms of displacement and virtual strain fields near the center of the crack obtained by the DIC method in Sect. 2. The displacement field near the crack center varies linearly in the normal direction, and the virtual principle strain distribution near the crack center in the normal direction is similar to the grayscale distribution of the laser stripe image. The optimized choice of parameters for the calculation is also provided in Sect. 2. Experiments are implemented to verify the accuracy of the theoretical derivation and measurements, and the results are shown in Sect. 3. Conclusions are given in Sect. 4.

2 Theoretical Analysis

2.1 Displacement Field

Brittle materials generally produce a very small elastic deformation under an external force when fracture occurs. Typical brittle materials include bricks, stones, ceramics, glass, and concrete. To facilitate the analysis, considering the mechanical properties of brittle materials, it is reasonable to assume that the displacements on both sides of the crack in a small range are a rigid body displacement.

As shown in Fig. 1, for Mode I crack, the displacement field is assumed to be the crack opening; while for Mode II crack, the displacement field is assumed to be the crack sliding. The displacement fields are expressed as

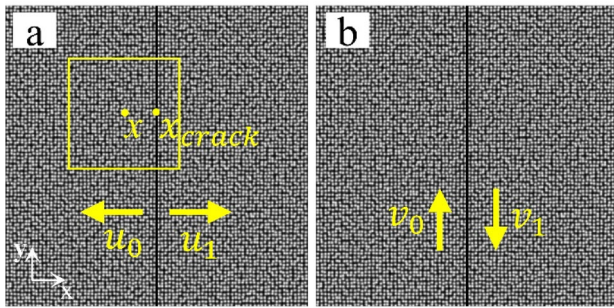


Fig. 1 a Crack opening for Mode I crack; b Crack sliding for Mode II crack

$$\text{opening} \begin{cases} u = u_0, x < x_{\text{crack}} \\ u = u_1, x > x_{\text{crack}} \\ v = 0 \end{cases}, \text{sliding} \begin{cases} v = v_0, x < x_{\text{crack}} \\ v = v_1, x > x_{\text{crack}} \\ u = 0 \end{cases} \quad (1)$$

For the convenience of analysis, the crack direction is parallel to the y -direction, and the displacement field changes solely in the x -direction. u_0 and u_1 are the displacements on the left and right sides of the opening mode I crack, respectively; v_0 and v_1 are the displacements on the left and right sides of the sliding mode II crack, respectively; x_{crack} is the coordinate of the crack in the x -direction; and x is the coordinate of the subset center.

When a first-order shape function is employed, the coordinates of each pixel can be expressed as Eqs. (2) and (3) in the local subset coordinate system in DIC, as illustrated in Fig. 2.

$$\begin{cases} x' = x + \xi_1(i, j, \vec{p}) = x_0 + i + \xi_1(i, j, \vec{p}) \\ y' = y + \eta_1(i, j, \vec{q}) = y_0 + j + \eta_1(i, j, \vec{q}) \end{cases} \quad (2)$$

$$\begin{cases} \vec{p} = (u, u_x, u_y)^T \\ \vec{q} = (v, v_x, v_y)^T \\ \xi_1(i, j, \vec{p}) = u + u_x i + u_y j \\ \eta_1(i, j, \vec{q}) = v + v_x i + v_y j \end{cases} \quad (3)$$

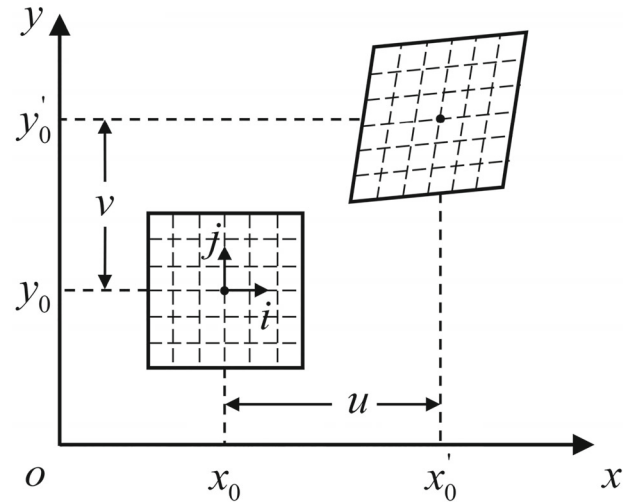


Fig. 2 Image coordinate system and local coordinate system centered at the subset

where (x, y) and (x_0, y_0) are the original coordinates and deformed coordinates of the subset center, respectively; (i, j) are the local coordinates of the subset; ξ_1 and η_1 are first-order shape functions; \vec{p} and \vec{q} are shape function parameters composed of the displacement of the subset center and the partial derivative of the displacement. According to the analysis in [33], the estimated displacement can be expressed by

$$\begin{cases} u^{\text{estimate}}(x, y) = \frac{1}{(2M+1)^2} \sum_{i, j=-M}^M u(x+i, y+j) \\ v^{\text{estimate}}(x, y) = \frac{1}{(2M+1)^2} \sum_{i, j=-M}^M v(x+i, y+j) \end{cases} \quad (4)$$

where $(2M+1)$ is the subset size. The step displacement field is fitted with a first-order shape function.

As shown in Fig. 1, when the coordinate of the subset center $x \in (x_{\text{crack}} - \frac{2M+1}{2}, x_{\text{crack}} + \frac{2M+1}{2})$, the subset intersects with the crack. The crack opening displacement fields, u and v , estimated by the first-order shape function are expressed as

$$\begin{cases} u^{\text{estimate}}(x, y) = \frac{u_0 - u_1}{2M+1}(x_{\text{crack}} - x) + \frac{u_0 + u_1}{2}, x \in \left(x_{\text{crack}} - \frac{2M+1}{2}, x_{\text{crack}} + \frac{2M+1}{2}\right) \\ v^{\text{estimate}}(x, y) = \frac{v_0 - v_1}{2M+1}(x_{\text{crack}} - x) + \frac{v_0 + v_1}{2}, x \in \left(x_{\text{crack}} - \frac{2M+1}{2}, x_{\text{crack}} + \frac{2M+1}{2}\right) \end{cases} \quad (5)$$

It indicates that the displacement changes linearly in a range of subset sizes near the crack.

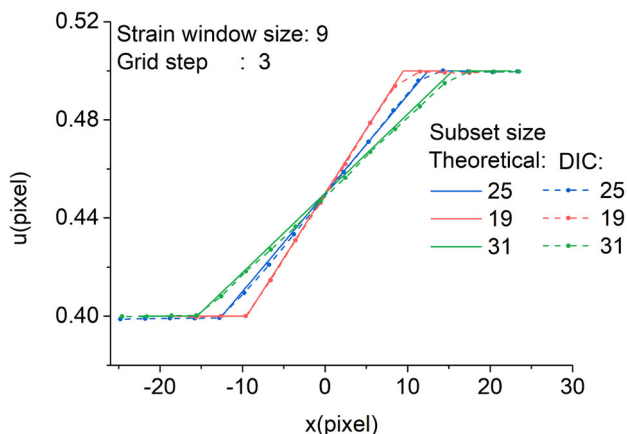


Fig. 3 Theoretical and simulated experimental results of crack opening displacements

Speckle images are generated to simulate real crack opening and sliding. As illustrated in Fig. 1a and b, the u -displacement difference between the left half and right half of the image is 0.1 pixel, and the v -displacement difference between the left half and right half of the image is also 0.1 pixel. The size of the simulated images is 512×512 pixels. When the size of the strain window is 9, and the step size is 3 pixels, the theoretical and simulated DIC results of different subset sizes are compared in Fig. 3. It is shown that the simulated DIC results agree well with the theoretical results. The higher the template is, the larger range of the displacement field is affected, and the simulated DIC results of displacement change linearly with the theoretical results.

2.2 Virtual Principle Strain Field

To calculate the strain tensor in DIC, displacements in the strain window with a size of $(2N + 1) \times (2N + 1)$ are fitted with a polynomial as

$$\begin{cases} u(x, y) = a_0 + a_1x + a_2y \\ v(x, y) = b_0 + b_1x + b_2y \end{cases} \quad (6)$$

where $a_0, a_1, a_2, b_0, b_1, b_2$ are the fitting coefficients, and x, y are the local coordinates of a point in the window [34]. The fitting formula of the strain window is obtained by the least squares method with a two-dimensional first-order polynomial, and the Cauchy strain components are calculated by the fitting coefficients as

$$\begin{cases} \varepsilon_x = \frac{\partial u}{\partial x} = a_1 \\ \varepsilon_y = \frac{\partial v}{\partial y} = b_2 \\ \gamma_{xy} = \frac{\partial u}{\partial y} + \frac{\partial v}{\partial x} = a_2 + b_1 \end{cases} \quad (7)$$

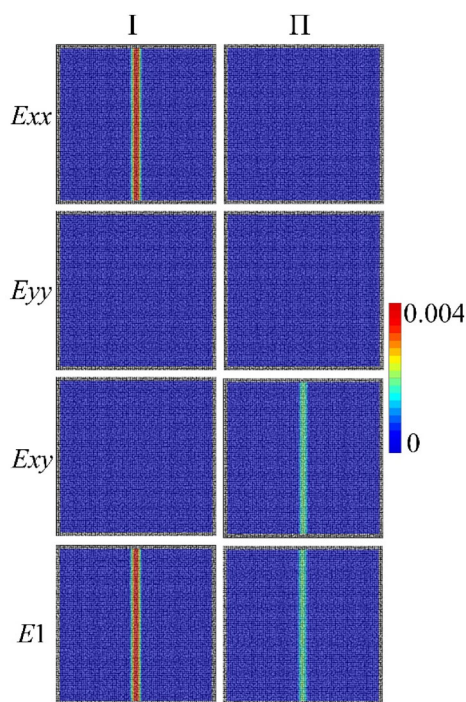


Fig. 4 Strain fields of DIC for crack opening and sliding

The principal strain of each point can be obtained by calculating the eigenvalue and eigenvector as

$$\varepsilon_1 = \frac{\varepsilon_x + \varepsilon_y}{2} + \sqrt{\left(\frac{\varepsilon_x - \varepsilon_y}{2}\right)^2 + \left(\frac{\gamma_{xy}}{2}\right)^2} \quad (8)$$

As illustrated in Fig. 4, the E_{xx} and E_1 fields can optimally reflect the Mode I crack propagation, crack opening; and the E_{xy} and E_1 fields can accurately reflect the Mode II crack propagation, crack sliding. Considering the unidirectionality of E_{xx}, E_{yy} , and E_{xy} , they may lose some crack opening or sliding information, while E_1 is the maximum strain in all directions of a point. Therefore, the principal strain field should be a suitable choice for further crack centerline extraction.

Considering the forms of the displacement fields of Mode I and Mode II cracks, the fitting plane problem of the strain window is reduced to a one-dimensional displacement field problem of straight-line fitting, which is expressed as

$$\begin{cases} u(x, y) = a_0 + a_1x \\ v(x, y) = b_0 + b_1x \end{cases} \quad (9)$$

$$\begin{cases} \arg \min \sum_{k=-N}^N (u(x_0 + Gk) - (a_0 + a_1x))^2 \\ \arg \min \sum_{k=-N}^N (v(x_0 + Gk) - (b_0 + b_1x))^2 \end{cases} \quad (10)$$

where G is the step size.

As illustrated in Fig. 5, regarding Mode I crack, the displacement field is linearly distributed near the crack center, the value of a_1 will be symmetric about the crack center, and solely the value of a_1 on the left side of the crack center needs to be considered. There should be two cases according to the strain window size ($2GN$) and subset size ($2M + 1$).

For Mode I crack, $E_{xx} \approx a_1$, $E_{yy} = 0$, $E_{xy} = 0$, and $E_1 = E_{xx}$. When $2GN < 2M + 1$, the theoretical formula of a_1 is derived as

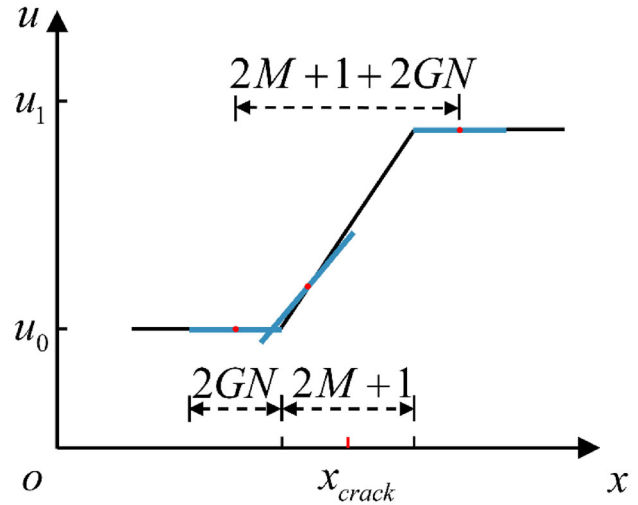


Fig. 5 Fitting displacement line with one-dimensional strain calculation window

$$\begin{cases} a_1(x) = \frac{u_1 - u_0}{(2M + 1)(2GN)^3} \left[-2 \left(x + GN + \frac{2M + 1}{2} - x_{crack} \right)^3 + 6GN \left(x + GN + \frac{2M + 1}{2} - x_{crack} \right)^2 \right], \\ x \in \left[x_{crack} - \frac{2M + 1}{2} - GN, x_{crack} - \frac{2M + 1}{2} + GN \right); \\ a_1(x) = \frac{u_1 - u_0}{(2M + 1)}, x \in \left[x_{crack} - \frac{2M + 1}{2} + GN, x_{crack} \right) \end{cases} \quad (11)$$

Because the strain window is smaller than the subset, the value of a_1 increases as a cubic function approaching the crack center and then remains at the maximum in a certain range near the crack center after reaching the peak value. The peak value can be estimated as

$$a_1(x)_{max} = a_1(x_{crack}) = \frac{u_1 - u_0}{(2M + 1)} \quad (12)$$

Similarly, the estimation of the value of b_1 can also be derived for Mode II crack with $E_{xx} = 0$, $E_{yy} = 0$, $E_{xy} = \frac{b_1}{2}$, and $E_1 = E_{xy}$.

When $2GN > 2M + 1$, the value of a_1 increases as a cubic function approaching the crack center initially and then increases as a quadratic function until reaching the peak value at the crack center, which is expressed as

$$\begin{cases} a_1(x) = \frac{u_1 - u_0}{(2M + 1)(2GN)^3} \left[-2 \left(x + GN + \frac{2M + 1}{2} - x_{crack} \right)^3 + 6GN \left(x + GN + \frac{2M + 1}{2} - x_{crack} \right)^2 \right], \\ x \in \left[x_{crack} - \frac{2M + 1}{2} - GN, x_{crack} + \frac{2M + 1}{2} - GN \right); \\ a_1(x) = \frac{u_1 - u_0}{(2GN)^3} \left[-6 \left(x + GN + \frac{2M + 1}{2} - x_{crack} \right)^2 + 6(2M + 1 + 2GN) \left(x + \frac{2M + 1}{2} + GN - x_{crack} \right) - 6(2M + 1)GN - 2(2M + 1)^2 \right], x \in \left[x_{crack} + \frac{2M + 1}{2} - GN, x_{crack} \right) \end{cases} \quad (13)$$

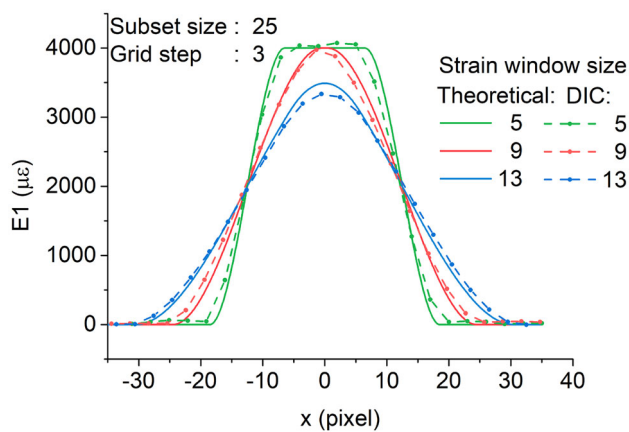


Fig. 6 Theoretical and simulated experimental results of virtual principle strain for crack opening

The peak value can be estimated as

$$a_1(x)_{\max} = a_1(x_{\text{crack}}) = \frac{u_1 - u_0}{16(GN)^3} \left(12(GN)^2 - (2M + 1)^2 \right) \tag{14}$$

Similarly, the estimation of the value of b_1 can also be derived for Mode II crack with $\varepsilon_x = 0, \varepsilon_y = 0, \gamma_{xy} = b_1$, and $\varepsilon_1 = \frac{\gamma_{xy}}{2}$.

As illustrated in Fig. 6, the abscissa of the crack center is assumed to be 0, and the subset and step sizes are set as 25 and 3 pixels, respectively. When the strain window size is $5 \times 5, 2GN < 2M + 1$, the values of the virtual principal strain fields are the maximum in a certain range near the crack center. When the strain window size is $13 \times 13, 2GN \geq 2M + 1$, the virtual principle strain field is maximal only at the crack center. The larger the size of the strain window is, the maximum virtual principle strain field is smaller when $2GN \geq 2M + 1$, and the larger the range of the virtual principle strain field is affected by the crack. Regarding Fig. 5, the range of the virtual principle strain field affected by the crack is $2M + 1 + 2GN$. The distribution of theoretical and simulated DIC results is both consistent with the above description, indicating that the simulated DIC results agree well with the theoretical ones.

In 3D-DIC, a local coordinate system must be established first to calculate the strain tensor. A set of $(2N + 1) \times (2N + 1)$ data points are employed around the calculation points to fit a local plane. The normal vector of the local plane can be determined according to the local plane equation, and the x -axis of the local coordinate system is obtained by the projection of the X_W -axis in the global coordinate system to the local plane. Subsequently, the normal vector is defined as the z -axis, and the y -axis is obtained from the relationship in the Cartesian coordinate system. After the local coordinates

are determined, the three-dimensional displacement is transformed from the global coordinates to the local coordinates. Finally, the displacement is fitted by a polynomial with the local least squares method similar to the 2D-DIC method. Therefore, this method of estimating the displacement and virtual principle strain field near the crack is still applicable to 3D-DIC.

2.3 Optimized Calculation Parameters for Crack Propagation Measurement

In our previous work, an accurate and automatic method was proposed for measuring the geometric parameters of crack propagation based on the virtual principal strain field and Steger’s algorithm [32]. Steger’s algorithm performs well when applied to the laser stripe which has a Gaussian distribution on the section. Before Steger’s algorithm [35] is applied to deal with the virtual principle strain field, it is necessary to select the appropriate subset size, step size, and strain window for DIC calculation to obtain the virtual principle strain field. As for the size of the strain window, it should not be smaller than the subset size ($2GN < 2M + 1$) for accurate crack center location. In addition, a smaller strain window introduces a larger strain noise [34], which significantly affects the accurate identification of small cracks. The range of the virtual principle strain field affected by the crack is approximately $2M + 1 + 2GN$ according to the analysis in Sect. 2.2. Therefore, the strain window and subset sizes should be moderate. Otherwise, the width of the virtual principle strain stripe will be too large, which may lead to the interaction of the virtual principle strain fields of the two cracks close to each other. Moreover, the smoothing effect of the strain window may lead to the loss of micro-crack information. The optimized choice of parameters for the calculation that can satisfy the equation $2M + 1 \approx 2GN$ is suggested.

Considering the distribution density of calculation points and calculation efficiency, the recommended DIC parameters for crack measurement in detail are as follows: subset size 25 pixels, step size 3 pixels, and strain window 9. Or subset size 21 pixels, step size 3 pixels, and strain window 7.

3 Experimental Verification

A crack propagation experiment is designed to verify the validity of the theoretical derivation and the accuracy of measurements. As illustrated in Fig. 7, the optimized digital speckle pattern [36] is affixed to the surfaces of the two glass plates. The glass plates on the right and left are fixed on the table and the translation platform, respectively. The translation platform is driven by a high-precision electric actuator of LTA-HS in the horizontal direction and fixed in the vertical and off-plane directions. The resolution of the camera is

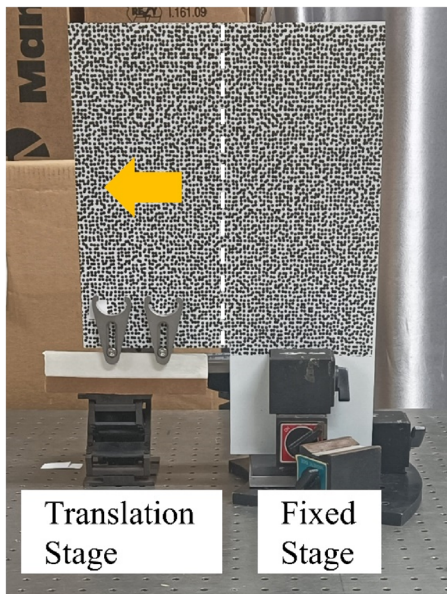


Fig. 7 Crack propagation experiment

2048×2048 pixels with a ratio of 3.62 pixel/mm. The actuator drives the left glass plate to move to the left and separates it from the right glass plate to simulate the crack propagation process. The actuator takes 30 steps, $5 \mu\text{m}/0.0181$ pixels at a time. The 2D-DIC and 3D-DIC systems are both set up to acquire images for DIC analysis simultaneously.

The virtual principle strain field related to the crack is partially submerged in the strain noise; hence, the minimum crack that can be identified by the crack identification method based on the virtual principle strain field is limited. To eliminate the interference of noise and other factors, a certain threshold should be applied, and it should be larger than the sum of the maximum elastic tensile strains of a certain material and the measured noise level of the virtual principle strain, which includes the mean and standard deviations of the virtual principle strain field.

In the crack propagation experiment, the mean value of the principal strain field noise is $300 \mu\epsilon$ with a standard deviation of $250 \mu\epsilon$, while the ultimate tensile strain of brittle materials in general is approximately hundreds of microstrain. A threshold greater than 3–5 times the standard deviation and the ultimate tensile strain should be applied before further processing to better locate the crack. Thus, a threshold of $1000 \mu\epsilon$ is applied to the principal strain field. As illustrated in Fig. 8, in both 2D-DIC and 3D-DIC systems, when the crack is very small (0.0181 pixel), the virtual principle strain field cannot reflect the entire crack. When the crack is 0.0362 pixel, the virtual principle strain field reflects the entire crack well. The smallest crack that can be detected by the virtual principle strain-based method under laboratory conditions is approximately 0.0362 pixel.

When the crack is 0.543 pixel, the experimental results of the deformation field near the crack are compared with the theoretical ones, as shown in Fig. 9a. The experimental results change linearly as the theoretical results; and the higher the template is, the larger range of the displacement field is affected. The experimental results of the virtual principal strain field are compared with the theoretical ones, as shown in Fig. 9b. The comparison between the experimental results and the theoretical results is similar to the comparison between the simulated DIC results and the theoretical results in Sect. 2, indicating that the experimental results are in good agreement with the theoretical ones, which proves the correctness of the proposed theory. Meanwhile, the results of Fig. 9 further prove the correctness of the optimized calculation parameters. When the subset size is 25 pixels and the grid step is 3 pixels, the recommended strain window size is 9 pixels.

The x -direction pixel coordinate of the crack in the image is 1253. The virtual principle strain fields calculated with the optimized parameters are processed using Steger's method.

As illustrated in Fig. 10a, the modulus of the crack center location error is less than 1 pixel for both 2D-DIC and 3D-DIC systems, and the standard deviation decreases and stabilizes with crack expansion. In particular, the standard deviation of center positioning for the 2D-DIC system reaches 3.8 pixels when measuring a small crack of 0.0362 pixel because the strain noise interfering significantly with the crack-induced virtual principal strain field. As the crack expands, the maximum virtual principal strain field caused by the crack is much larger than the noise; therefore, the center location error and standard deviation decrease. As illustrated in Fig. 10b, the measurement error of the crack width for the 2D-DIC and 3D-DIC systems gradually increases with the crack extension, but it is less than 0.025 pixel for 2D-DIC and 0.02 pixel for 3D-DIC, and the standard deviations are both less than 0.01 pixel, which is consistent with the accuracy of the DIC. The experimental results illustrate that the crack measurement method based on the virtual principal strain field has high accuracy of crack center location with an error less than 2 pixels when the crack width is larger than 0.15 pixel, and very high accuracy of crack width measurement with an error less than 0.025 pixel.

4 Conclusion

To practically and accurately measure the geometric parameters of crack propagation, this study first theoretically analyzed the distribution of displacement and virtual principal strain field in the section of cracks and discussed the influences of subset size, step and strain window. The theoretical equations of virtual principal strain field were given. The effectiveness of the derived theoretical equations was

Fig. 8 **a** 2D-DIC-based virtual principle strain field under different thresholds; **b** 3D-DIC-based virtual principle strain field under different thresholds

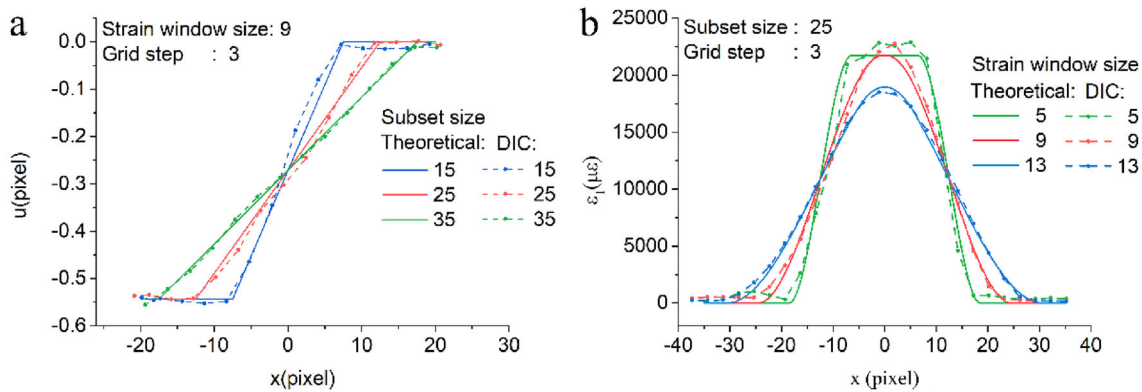
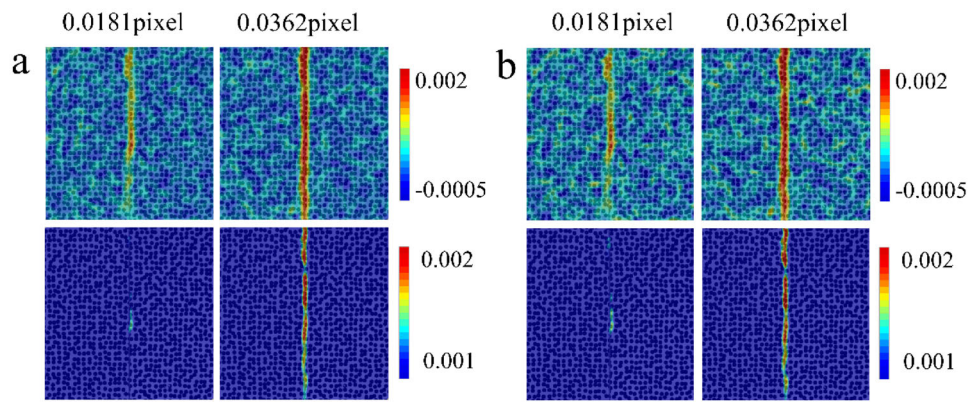


Fig. 9 **a** Theoretical and experimental results of displacement; **b** theoretical and experimental results of virtual principle strain field

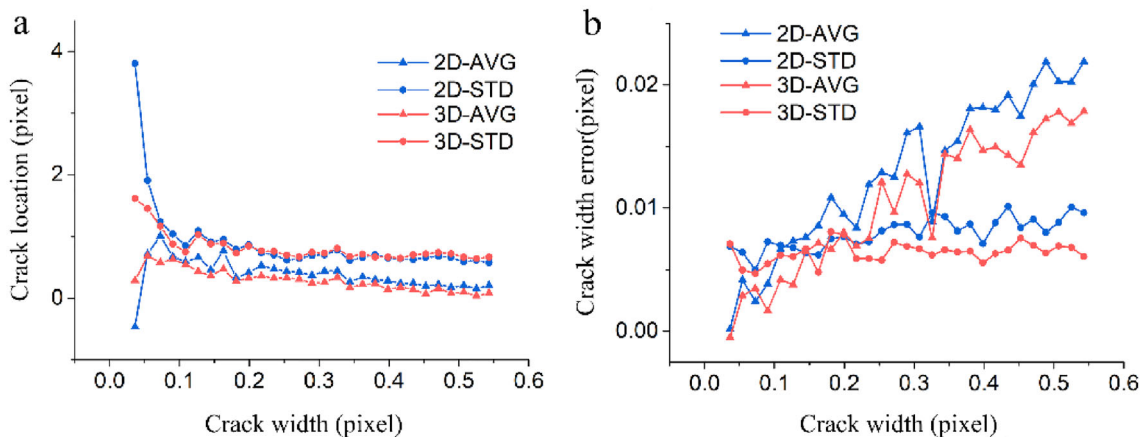


Fig. 10 **a** Crack center location accuracy; **b** crack width accuracy

well verified by the simulation experiments and real experiments. According to the theoretical equations, it is shown that the virtual principle strain keeps the maximum in a certain range near the crack center when $2GN < 2M + 1$. While the virtual principle strain is maximal only at the crack center when $2GN \geq 2M + 1$. The peak value of the virtual principle strain field is estimated using Eq. (12).

According to the theoretical analysis, the optimized choice of parameters for calculation that can satisfy the equation $2GN \approx 2M + 1$ is suggested for crack propagation measurement based on the virtual principal strain field and Steger's algorithm. With the optimized calculation parameters, the minimum crack that can be measured by the proposed method in this study is approximately 0.0362 pixel, while the measurement error of the crack width is less than 0.025 pixel.

Acknowledgements This study was supported by the National Natural Science Foundation of China (NSFC) (11902074).

Data Availability The data that support the findings of this study are available from the corresponding author upon reasonable request.

Declarations

Conflict of interest The authors declare that they have no conflict of interest.

References

- Ritchie RO, Thompson AW. On macroscopic and microscopic analyses for crack initiation and crack growth toughness in ductile alloys. *Metall Trans A*. 1985;16(2):233–48.
- Wu C, Zhao W, Beck T, Peterman R. Optical sensor developments for measuring the surface strains in prestressed concrete members. *Strain*. 2011;47:e376–86.
- Abdel-Qader L, Abudayyeh O, Kelly M. Analysis of edge-detection techniques for crack identification in bridges. *J Comput Civil Eng*. 2003;17(4):255–63.
- Zhou J, Huang P, Chiang F. Wavelet-based pavement distress classification. *Transp Res Record*. 2005;1940:89–98.
- Ying L, Salari E. Beamlet transform-based technique for pavement crack detection and classification. *Comput-Aided Civil Infrastruct Eng*. 2010;25(8):572–80.
- Shu Z, Guo Y. Algorithm on contourlet domain in detection of road cracks for pavement images. *J Algo Comput Technol*. 2013;7(1):15–25.
- Ni F, Zhang J, Chen Z. Pixel level crack delineation in images with convolutional feature fusion. *Struct Control Health Monit*. 2019;26(1):e2286.
- Zou Q, Zhang Z, Li Q, Qi X, Wang Q, Wang S. DeepCrack: learning hierarchical convolutional features for crack detection. *IEEE Trans Image Process*. 2018;28(3):1498–512.
- Cha Y, Choi W, Buyukozturk O. Deep learning-based crack damage detection using convolutional neural networks. *Comput-aided Civil Infrastruct Eng*. 2017;32(5):361–78.
- Peters W, Ranson W. Digital image techniques in experimental stress-analysis. *Opt Eng*. 1982;21(3):427–31.
- Yamaguchi I. A laser-speckle strain-gauge. *J Phys E*. 1981;14(11):1270–3.
- Bruck H, McNeill S, Sutton M, Peters W. Digital image correlation using Newton-Raphson method of partial differential correction. *Exp Mech*. 1989;29:261–7.
- Sutton M, Ke X, Lessner S, Goldbach M, Yost M, Zhao F, Schreier H. Strain field measurements on mouse carotid arteries using microscopic three-dimensional digital image correlation. *J Biomed Mater Res Part A*. 2008;84A(1):178–90.
- Xie H, Yang W, Kang Y, Zhang Q, Han B, Qiu W. *In-situ* strain field measurement and mechano-electro-chemical analysis of graphite electrodes via fluorescence digital image correlation. *Exp Mech*. 2021;61:1249–60.
- Xing T, Zhu H, Liu G, Song Y, Ma S. Global mechanical behavior characterization of uniaxially loaded rock specimen based on its structural evolution. *Appl Sci-Basel*. 2020;10(21):7647.
- Sheng Z, Chen B, Hu W, Yan K, Miao H, Zhang Q, Yu Q, Fu Y. LDV-induced stroboscopic digital image correlation for high spatial resolution vibration measurement. *Opt Express*. 2021;29(18):34–28147.
- Zhu J, Xie H, Hu Z, Chen P, Zhang Q. Residual stress in thermal spray coatings measured by curvature based on 3D digital image correlation technique. *Surf Coat Technol*. 2011;206:1396–402.
- Gao Z, Li F, Liu Y, Cheng T, Su Y, Fang Z, Yang M, Li Y, Yu J, Zhang Q. Tunnel contour detection during construction based on digital image correlation. *Opt Lasers Eng*. 2020;126:105879.
- Poissant J, Barthelat F. A novel subset splitting procedure for digital image correlation on discontinuous displacement fields. *Exp Mech*. 2010;50(3):353–64.
- Hassan G, Dyskin A, MacNish C, Pasternak E, Shufrin I. Discontinuous digital image correlation to reconstruct displacement and strain fields with discontinuities: dislocation approach. *Eng Fract Mech*. 2018;189:273–92.
- Rthor J, Roux S, Hild F. From pictures to extended finite elements: extended digital image correlation (x-dic). *C R Mec*. 2007;335(3):131–7.
- Rthor J, Tinnes J, Roux S, Buffire J, Hild F. Extended three-dimensional digital image correlation (X3D-DIC). *C R Mec*. 2008;336(8):643–9.
- Han J, Pan B. A novel method for measuring discontinuous deformation in digital image correlation based on partition and dividing strategy. *Eng Fract Mech*. 2018;204:185–97.
- Yuan F, Cheng L, Shao S, Dong Z, He X. Full-field measurement and fracture and fatigue characterizations of asphalt concrete based on the SCB test and stereo-DIC. *Eng Fract Mech*. 2020;235:107127.
- Alam S, Loukili A, Grondin F, Rozière E. Use of the digital image correlation and acoustic emission technique to study the effect of structural size on cracking of reinforced concrete. *Eng Fract Mech*. 2015;143:17–31.
- Ruocci G, Rospars C, Bisch P, Erlicher S, Moreau G. Cracks distance and width in reinforced concrete membranes: experimental results from cyclic loading histories. 15th World Conference on Earthquake Engineering, Lisbon, Portugal 2012; pp. 1278–84.
- Ruocci G, Rospars C, Moreau G, Bisch P, Erlicher S, Delaplace A, Henault JM. Digital image correlation and noise-filtering approach for the cracking assessment of massive reinforced concrete structures. *Strain*. 2016;52:503–21.
- Shih M, Sung W. Application of digital image correlation method for analyzing crack variation of reinforced concrete beams. *Sadhana*. 2013;38:723–41.
- Ghorbani R, Matta F, Sutton M. Full-field deformation measurement and crack mapping on confined masonry walls using digital image correlation. *Exp Mech*. 2015;55:227–43.
- Rajan S, Sutton M, Rizos D, Ortiz A, Zeitouni A, Caicedo J. A stereovision deformation measurement system for transfer length estimates in prestressed concrete. *Exp Mech*. 2018;58:1035–48.
- Gehri N, Mata-Falcón J, Kaufmann W. Automated crack detection and measurement based on digital image correlation. *Constr Build Mater*. 2020;256:119383.
- Gu L, Gong W, Shao X, Chen J, Dong Z, Wu G, He X. Real time measurement and analysis of full surface cracking characteristics of concrete based on principal strain field. *Chin J Theor Appl Mech*. 2021;53(7):1962–70.
- Xu X, Su Y, Zhang Q. Theoretical estimation of systematic errors in local deformation measurements using digital image correlation. *Opt Lasers Eng*. 2017;88:265–79.
- Pan B, Asundi A, Xie H, Gao J. Digital image correlation using iterative least squares and pointwise least squares for displacement field and strain field measurements. *Opt Lasers Eng*. 2009;47(7–8):865–74.
- Steger C. An unbiased detector of curvilinear structures. *IEEE Trans Pattern Anal Mach Intell*. 1998;20(2):113–25.
- Chen Z, Shao X, Xu X, He X. Optimized digital speckle patterns for digital image correlation by consideration of both accuracy and efficiency. *Appl Opt*. 2018;57(4):884–93.